Journal of Alloys and Compounds 690 (2017) 63–71

Contents lists available at ScienceDirect

Journal of Alloys and Compounds

journal homepage: http://www.elsevier.com/locate/jalcom

High emissivity $MoSi_2$–$TaSi_2$–borosilicate glass porous coating for fibrous ZrO_2 ceramic by a rapid sintering method

Gaofeng Shao [a, b], Xiaodong Wu [a, b], Sheng Cui [a, b, **], Xiaodong Shen [a, b, *], Yucao Lu [a, b], Qinhao Zhang [a], Yong Kong [a, b]

[a] State Key Laboratory of Materials–Oriented Chemical Engineering, College of Materials Science and Engineering, Nanjing Tech University, Nanjing 210009, China
[b] Jiangsu Collaborative Innovation Center for Advanced Inorganic Function Composites, Nanjing 210009, China

ARTICLE INFO

Article history:
Received 28 June 2016
Received in revised form
8 August 2016
Accepted 9 August 2016
Available online 12 August 2016

Keywords:
High emissivity coating
Fibrous ceramic
Rapid sintering method
Thermal shock behavior

ABSTRACT

A $MoSi_2$-$TaSi_2$-borosilicate glass porous coating was designed and prepared on fibrous ZrO_2 ceramic with slurry dipping and subsequent rapid sintering method. The microstructure, radiative property and thermal shock behavior of the coating have been investigated. The results show the coating presents a top Ta-Si-O compound glass layer and a porous $MoSi_2$-$TaSi_2$-borosilicate glass inner layer. The total emissivity of the coating is up to 0.88 in the range of 0.3–2.5 μm and 0.87 in the range of 2.5–15 μm at room temperature. The increased surface roughness leads to the increased emissivity, which can be explained by "V-shaped grooves" model. The coating turns into a dense structure and presents an interlocking structure in the interfacial layer after thermal cycling between 1673 K and room temperature 10 times, exhibiting excellent thermal shock resistance, which was attributed to the synergistic effect of porous structure and the match of thermal expansion coefficient between the coating and substrate.

Reusable launch vehicles (RLVs), such as the space shuttle, repeatedly travel into or beyond, the earth's upper atmosphere and then return to the earth's surface. During fight, the RLVs experience extreme temperatures upon reentry to the atmosphere. Because of the extreme temperatures, the vehicle and its contents must be protected by a reusable thermal protective system, which consisting of a high emissivity coating used on the surface and a low thermal conductivity insulation used inside [1]. In the past decades, the most predominate low density and low thermal conductivity insulations are Lockheed Insulation (LI) and Alumina Enhanced Thermal Barrier (AETB) [2]. In recent ten years, hybrid aerogel rigid ceramic fiber insulation materials are springing up [3–5]. Recently, porous fibrous ZrO_2 ceramics with bird's nest–like structure have drawn more attention due to the advantages of low density, extreme high–temperature stability and low thermal conductivity, which is considered as a candidate material for thermal insulation under conditions of ultra–high temperatures and in various severe environments [6]. Alfano et al. stated that radiation heat transfer is the only method for heating and cooling in outer space application [7]. Furthermore, a mathematical model proposed by Van Wie suggested that under identical heat flux the wall temperature of a hypersonic vehicle is reduced by 573 K when its surface emissivity is increased from 0.5 to 1.0 at Mach 10 [8]. Thus, a high emissivity coating must be designed and prepared on the fibrous ZrO_2 ceramic insulation substrate, which is desired to maximize the amount of heat radiated from the surface.

Generally, the high emissivity coating comprises of at least two phase: a crystalline phase and an amorphous phase, or two different crystalline phases, in which at least one is capable of absorbing and re-radiating thermal energy(emissivity agents) [9]. In the group of silicide–based compounds, transition metal disilicides such as $MoSi_2$ and $TaSi_2$ possess attractive combined properties, including high melting point ($MoSi_2$: 2293 K, $TaSi_2$: 2473 K), relatively low density ($MoSi_2$: 6.24 g/cm^3, $TaSi_2$: 9.14 g/cm^3) [10], acceptable mechanical property and excellent oxidation resistance in air. They were mainly researched in the fields of the

* Corresponding author. State Key Laboratory of Materials–Oriented Chemical Engineering, College of Materials Science and Engineering, Nanjing Tech University, Nanjing 210009, China.
** Corresponding author. State Key Laboratory of Materials–Oriented Chemical Engineering, College of Materials Science and Engineering, Nanjing Tech University, Nanjing 210009, China.
E-mail addresses: scui@njtech.edu.cn (S. Cui), xdshen@njtech.edu.cn (X. Shen).

http://dx.doi.org/10.1016/j.jallcom.2016.08.073
0925-8388/

oxidation protective coatings for carbon/carbon composites [11–14] and the sintering aids for improving the densification of ultra–high–temperature–ceramics [15,16]. However, high emissivity coating which utilizes $MoSi_2$ or $TaSi_2$ as high emissivity additives for low conductivity insulation is limited. In our previous study, the emissivity of $MoSi_2$ based coating is only 0.8 [17]. Though the emissivity value of $TaSi_2$ based coating could reach at 0.9, the thermal shock resistance was unacceptable [18]. Since $MoSi_2$ and $TaSi_2$ own different properties in the coating, both addition of $MoSi_2$ and $TaSi_2$ is promising to further improve radiative property and thermal shock resistance by right of the synergistic effect of $MoSi_2$ and $TaSi_2$. The amorphous phase is like a binder which can be coupled with good bonding characteristic to the porous substrate, provide strength and tailor their thermal expansion characteristic between the coating and the substrate, such as colloidal silicon dioxide and borosilicate glass [19]. Additionally, the expected oxidation products of $TaSi_2$, SiO_2 and Ta_2O_5 have melting points of 2000 K and 2145 K, which could exist as immiscible phases in the borosilicate or silicate glass, which not only can increase the viscosity and stability of the glass layer, but also can reduce their oxygen diffusion rates [13,20].

To date, many methods such as pack cementation [13,21], in situ reaction [14] and plasma spray [22,23] have been developed to prepare $MoSi_2$ and $TaSi_2$ based coating for various substrates. However the pack cementation and in situ reaction method need high temperature conditions (above 2073 K) and long sintering time (more than 2 h), plasma spray needs expensive deposition techniques. The slurry and subsequent rapid sintering method has been developed to prepare glass based coating for fibrous ceramic [17,24] and carbon-bonded carbon fiber composites [25], taking the advantage of the softened and molten properties of the glass in high temperature.

Furthermore, considering the porous structure of ZrO_2 ceramic substrate, a similar porous coating should be designed, which could relax the thermal shock stress, arrest the propagation of micro cracks effectively and improve the thermal shock resistance. In the previous studies, Fe_2O_3 was used as pore-forming agent in the coating for C/C composite to improve the ablation resistance [26]. Ferrocene addition increased the porosity of ZrB_2-SiC coating for graphite and improved the thermal shock resistance [27]. Moreover, B_2O_3 content in $MoSi_2$-BaO-Al_2O_3-SiO_2 coating was adjusted to prepare the gradient porous structure, which had better bonding strength and thermal shock resistance [19].

In this work, $MoSi_2$ and $TaSi_2$ are synchronous introduced as the emittance agents and the suitable content borosilicate glass is controlled as binder to prepare the porous $MoSi_2$–$TaSi_2$–borosilicate glass porous coating by the dipping slurry and subsequent sintering method on fibrous ZrO_2 ceramic insulation. The microstructure, radiative property and thermal shock behavior were investigated, as well as the thermal shock mechanism.

1. Experimental

1.1. Preparation of the coatings

Fibrous ZrO_2 ceramics (25 mm × 25 mm × 5 mm and 15 mm × 15 mm × 5 mm) (Anhui Crystal New Materials Co. Ltd., China) were used as the substrates. The large size substrates (25 mm × 25 mm × 5 mm) were used for radiation property test, while the small size substrates (15 mm × 15 mm × 5 mm) were used for thermal shock test. The microstructure of the fibrous ZrO_2 ceramic is shown in Fig. 1(a). It can be observed that the fibrous ZrO_2 ceramic can form a " bird's nest " structure to obtain high porosity, low thermal conductivity and relatively high strength. Fig. 1(b) shows the pore size distribution of fibrous ZrO_2 ceramic determined by mercury intrusion method. The curve presents a single peak (36.86 μm) with a narrow width, signifying uniform pore size distribution.

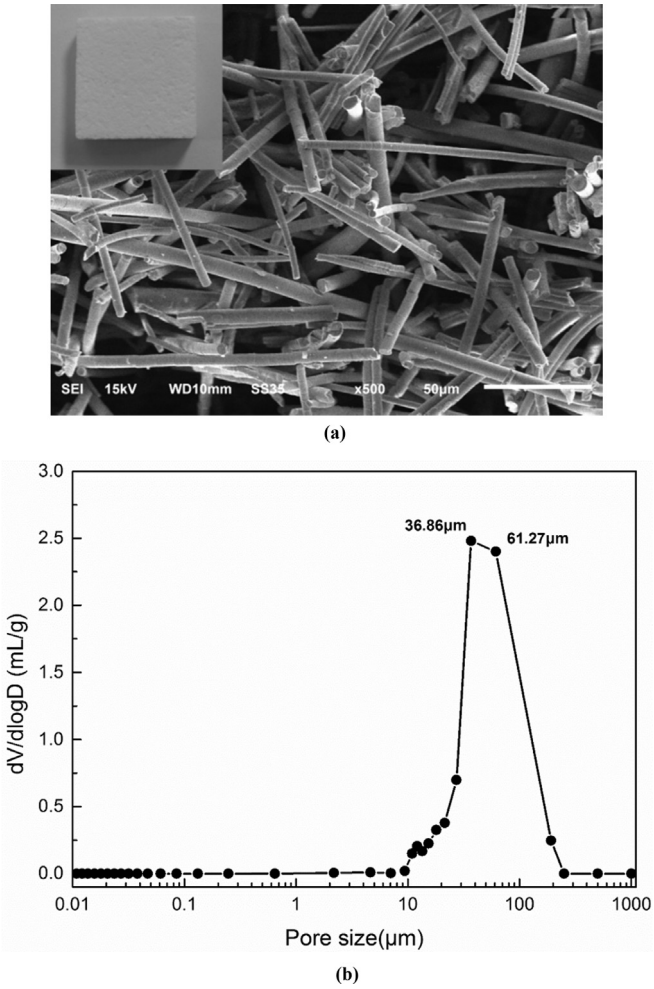

Fig. 1. (a) The SEM image of fibrous ZrO_2 ceramic (inset refers to the photograph of fibrous ZrO_2 ceramic); (b) Pore size distribution of fibrous ZrO_2 ceramic.

A slurry was pre–prepared by a method of ball milling. $MoSi_2$ (55 wt%) and $TaSi_2$ (25 wt%) (Beijing HWRK Chem Co., Ltd, China), borosilicate glass (20 wt%), ethanol and silica sol were mixed in a nylon ball–milling container and ball milled by a planetary mill for 6 h at a rotation speed of 400 rpm, where the mass ratio of the powders, ethanol, silica sol and zirconia balls = 1:1:0.1:2. Eventually, the particle size reached approximately 1–2 μm and the reduced particle size allowed effective impregnation of the outer surface. The coating was prepared on the surface of the treated fibrous ZrO_2 ceramic using the dip–coating process. The coating thickness was controlled by the dipping times. After drying at 333 K for 4 h and at 373 K for 2 h, the as–coated samples were then inserted into the furnace at 1573 K in air and cooled by rapid removal from the furnace at atmospheric pressure.

1.2. Radiation property test

For most practical purposed, thermal radiation is concerned with a wavelength range of 0.1–100 μm, including the ultraviolet and visible (λ = 0.1–0.8 μm), near infrared (λ = 0.8–10 μm), and far infrared (λ = 10–20 μm) spectra [28]. Thus, reflectance spectra in the 0.3–2.5 μm wavelength range were measured using a

UV–vis–NIR spectrophotometer (UVPC measurement software, Shimadzu; Varian Cary 5000, Varian), with $BaSO_4$ as the reflectance sample. The diffused spectra in the 2.5–15 μm wavelength range were obtained with FT–IR spectrometer (Frontier, PerkinElmer LLC) equipped with a gold–coated integrating sphere. With reflection measurement methods the emissivity (absorptivity) is obtained indirectly from the measured reflectance based on the relation for materials, ε = A = 1-R-T: ε, A, R and T being the emissivity, absorptivity, reflectivity, and transmissivity respectively. The total emissivity can be derived from the reflectance spectrum according to Eq. (1)

$$\varepsilon_T = \frac{\int_{\lambda_1}^{\lambda_2}[1 - R(\lambda)]P_B(\lambda)d\lambda}{\int_{\lambda_1}^{\lambda_2} P_B(\lambda)d\lambda} \quad (1)$$

Where λ is the wavelength, $R(\lambda)$ is the reflectance, $P_B(\lambda)$ is given by Planck's law, which is calculated according to Eq. (2):

$$P_B(\lambda) = \frac{C_1}{\lambda^5[\exp(C_2/\lambda T) - 1]} \quad (2)$$

where$C_1 = 3.743 \times 10^{-16}\ Wm^2$, $C_2 = 1.4387 \times 10^{-2}\ mK$[29]. The calculation of the total emissivity was performed using a MATLAB program that incorporated Eqs. (1) and (2).

1.3. Determination of surface parameters

In order to provide a numerical evaluation of the surface, the asperity height of the roughness profile is quantified by amplitude parameters (such as *Rq, Rsk* etc …), and all expressed in micrometers. The root mean square roughness (*Rq*) calculates the root mean square average of the profile deviation from the mean line (i.e., the standard deviation of the height distribution): $Rq = \sqrt{\frac{1}{n}\sum_{i=1}^{n} Z_i^2}$ The skewness of the profile (*Rsk*) is the quotient of the mean cube value of the ordinate values z(x) and the cube of Rq within the evaluation length: $Rsk = \frac{1}{R_q^3}\left(\frac{1}{n}\sum_{i=1}^{n} z_i^3\right)$, which provides a description of the asymmetry of the profile and it is close to zero for a Gaussian height distribution, whereas a positive values is indicative of a flat surface with peaks, and a negative value a bearing surface with valleys [30].

1.4. Thermal shock behavior

To investigate the thermal shock resistance of the coating, thermal cycling tests of coated specimens were performed between 1673 K and room temperature in air. Specimens were put directly into the furnace of specific for 10 min, and then were taken out of the furnace for 10 min. Then, the specimens were put directly into the furnace again for the next thermal cycle, and the total number of thermal cycle is 10. At the designated time, the weight of these specimens was measured by the electronic balance with a sensitivity of ±0.1 mg. Weight change percentage ($\Delta W\%$) of the specimens was calculated by the following equation: $\Delta W\% = \frac{m_0 - m_1}{m_0} \times 100\%$ (3), where m_0 and m_1 are the weights of the specimens before oxidation and after oxidation, respectively.

1.5. Thermal expansion coefficient test

The linear thermal expansion behaviors of fibrous ZrO_2 ceramic, $MoSi_2$ and $TaSi_2$ using the bulk specimens have dimensions of approximately 4 mm × 5 mm × 20 mm were determined with a high-temperature dilatometer (Netzsch DIL 402C, Germany) from 323 K to 1673 K in Ar atmosphere. Data was continuously recorded at a heating rate of 10 K/min during heating, and they were corrected using the known thermal expansion of a certified standard alumina.

1.6. Characterization of the coatings

The surface morphology was examined using a confocal laser scanning microscope (CLSM). The CLSM images were obtained on an Olympus LEXT OLS 4000 microscope powered by a singer laser (λ = 405 nm) in the reflected light mode. The microstructure and the element distribution were surveyed using a scanning electron microscope (SEM, Model JSM–6510, JEOL, Tokyo, Japan) equipped with energy dispersive spectroscopy (EDS). The phase composition of feedstock and the coating surface were examined using a Rigaku Miniflex X–ray diffractometer (XRD) with Cu–Kα radiation (λ = 0.15406 nm).

2. Result and discussion

2.1. Microstructure of the coating

Fig. 2 presents the XRD patterns of the feedstock powders and the surface of as–prepared $MoSi_2$–$TaSi_2$–borosilicate glass coating. As shown in Fig. 2(a), $MoSi_2$ and $TaSi_2$ diffraction peaks with strong intensity can be detected in feedstock powders, meanwhile the amorphous nature of glass near 22° can be observed, indicating that the borosilicate glass is included. Besides of the phases of $MoSi_2$, $TaSi_2$ and borosilicate glass, Mo_5Si_3, Mo and MoO_2 are also recognized in as–prepared coating surface, which are responsible for the formation of the oxidation products of $MoSi_2$ based on Eqs (4), (7) and (8). It is well known that different oxidation products will be generated at different oxygen partial pressures (P_{O2}). In fact, the formation of MoO_3 is commonly observed in the initial oxidation of $MoSi_2$, but the MoO_3 layer offers no protection to continued oxidation and MoO_3 is the most volatile phase in the PO_2 range $1–10^5$ Pa at 1473 K. And the borosilicate glass phase does restrict oxygen transport and provides a reduced oxygen activity so that MoO_2 and Mo form, which are the stable phases for the PO_2 range

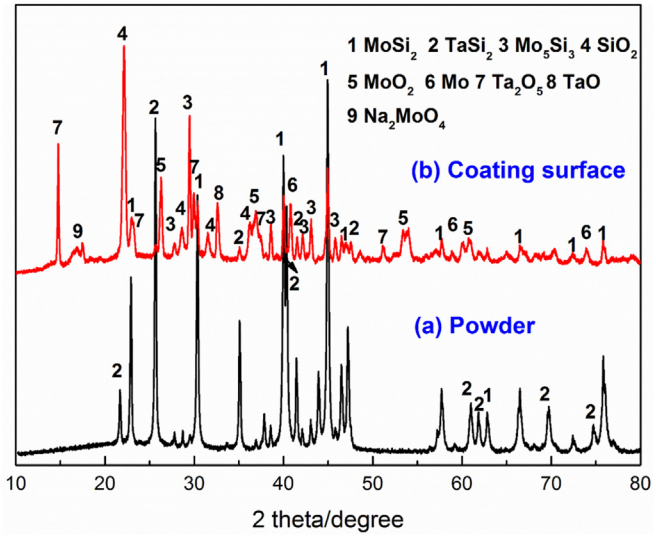

Fig. 2. XRD patterns of (a) original powders and (b) The surface of $MoSi_2$–$TaSi_2$–borosilicate glass coating.

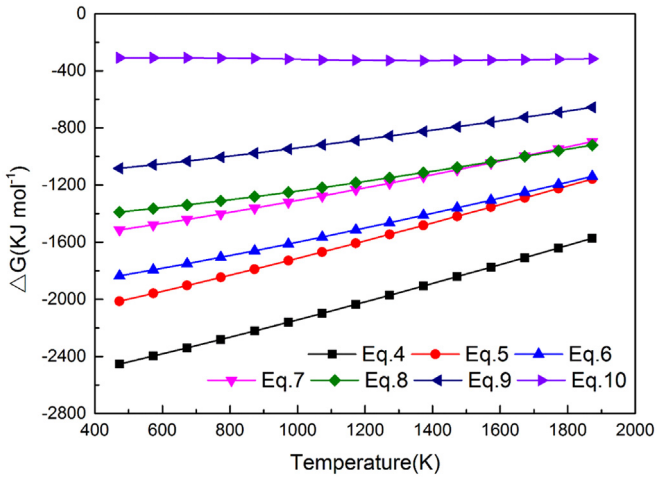

Fig. 3. Gibbs-free energy for reactions (4)–(10) as described in Section 2.1 of the text.

10^{-6}–1 Pa and $PO_2 < 10^{-6}$ Pa [31]. Moreover, TaO and Ta_2O_5 phases are supposed to form from the products of the sight oxidation of $TaSi_2$ based on Eqs. (5) and (9) during the preparation process of the coating. The crystalline SiO_2 is not formed only the oxidation of $MoSi_2$ and $TaSi_2$ during the soaking at 1573 K according to Eqs. (4)–(9) but also from the partial borosilicate glass crystallized during the following cooling process. Additionally, Na_2MoO_4 diffraction peak with week intensity is detected near 17°, which is obtained through the reaction between Na_2O and MoO_3 according to Eq. (10). As shown in Fig. 3, the Gibbs–free energy, △G, for reactions (4)–(10) at temperatures ranging from 473 K to 1873 K is calculated by the FACT program. Negative △G demonstrates that these reactions are thermodynamically favorable and can occur under the heat–treatment process.

$$MoSi_2(s) + 7/5O_2(g) = 1/5Mo_5Si_3(s) + 7/5SiO_2(g) \quad (4)$$

$$TaSi_2(s) + 5/2O_2(g) = TaO(s) + 2SiO_2(s) \quad (5)$$

$$MoSi_2(s) + 7/2O_2(g) = MoO_3(g) + 2SiO_2(s) \quad (6)$$

$$MoSi_2(s) + 2O_2(g) = Mo(s) + 2SiO_2(s) \quad (7)$$

$$MoSi_2(s) + 3O_2(g) = MoO_2(s) + 2SiO_2(s) \quad (8)$$

$$TaSi_2(s) + 13/4O_2(g) = 1/2Ta_2O_5(s) + 2SiO_2(s) \quad (9)$$

$$Na_2O \text{ (most stable)} + MoO_3 \text{ (most stable)} = Na_2MoO_4 \text{(most stable)} \quad (10)$$

Fig. 4 (a) shows the macrograph of the as–prepared $MoSi_2$–$TaSi_2$–borosilicate glass coated fibrous ZrO_2 ceramic. The CLSM image of the surface of the coating is presented in Fig. 4 (b), which is glossy, dense, without micro cracks and with an "island" structure. Fig. 4 (c) shows the magnification of region A in Fig. 4(b), and the SEM image of corresponding region A is shown in Fig. 4(e). By the EDS analysis, the surface comprises of Ta, Si and O elements, which suggests that a Ta– Si– O glass layer is generated in the surface of the coating. Fig. 4(d) shows the magnification of region B in Fig. 4(b), from which it can be seen that the transparent particles exist as "immiscible phases" embedded the continuous glass phase, and the corresponding SEM image is shown in Fig. 4(f), which presents dispersed cluster configuration. It has been reported that the transition metal oxides exist as "immiscible phases" in the borosilicate or silicate glass, which not only can increase the viscosity and stability of the glass layer, but also can reduce their oxygen diffusion rates [32]. Thus, a compound glass layer generated during the prepare process could act as an oxidation resistance layer.

Fig. 5(a) shows the cross–section SEM micrograph of the fibrous ZrO_2 ceramic coated $MoSi_2$–$TaSi_2$–borosilicate glass coating. The coating consists of two parts: surface coating layer (zone I) and interfacial transition layer (zone II). The surface coating layer displays a porous structure with the thickness of approximately 150 μm, which is clearly shown in magnified SEM image (Fig. 5(b)). In the interfacial transition layer, part of the coating material has infiltrated into the substrate through the open pores of fibrous ZrO_2 ceramic insulation and combined ZrO_2 fiber well through the continuous glass phase. Therefore, the obtained coating has an excellent combination with the substrate, and no obvious delamination is discovered between the coating and the substrate, which is beneficial to increasing the compatibility and adherence between the coatings and the substrate. Fig. 5(c) shows the cross–section backscatter micrograph of the $MoSi_2$–$TaSi_2$–borosilicate glass coating. On the top of the coating, there exists a grey layer with the thickness of 10 μm

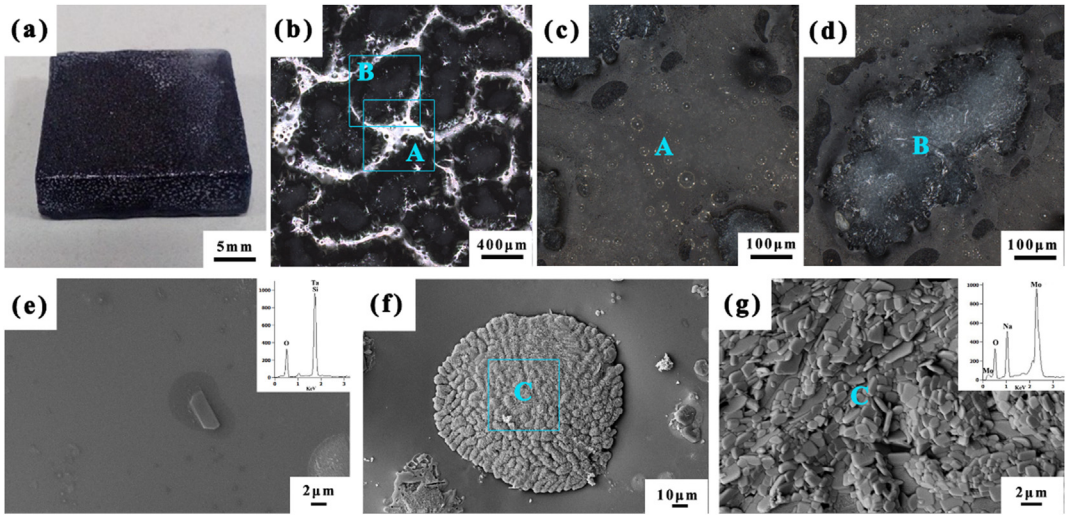

Fig. 4. (a) Macrograph of the as–prepared $MoSi_2$–$TaSi_2$–borosilicate glass coated fibrous ZrO_2 ceramic; (b–d) The CLSM images of the coating; (e–g) The SEM images of the coating.

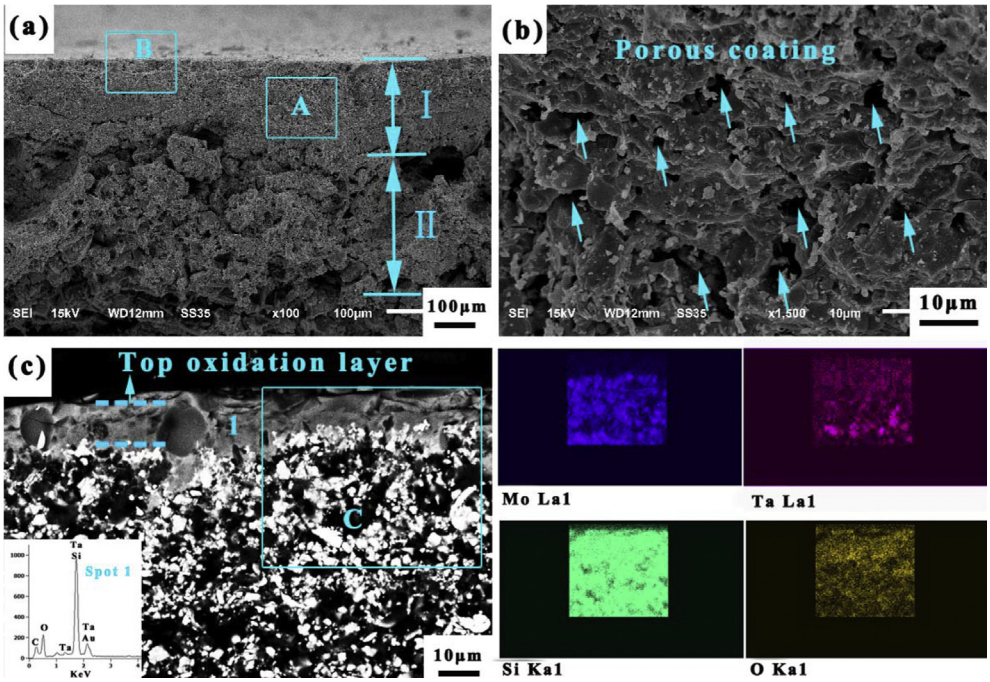

Fig. 5. (a) Cross–section SEM micrograph of the fibrous ZrO_2 ceramic coated $MoSi_2$–$TaSi_2$–borosilicate glass coating; (b) magnification of region A; (c) Polished cross–section BSE micrograph of the coating about region B and element distribution maps of region C.

approximately which is marked with two blue lines. By EDS analysis, it can be seen that the top layer mainly consisted of O, Si and Ta elements, which can be recognized as Ta–Si–O glass layer. Correspondingly, the element distribution map of Mo also verifies the thimbleful of Mo in the top oxidation layer. At the same time, Ta, Si and O are uniformly distributed in the coating. Fig. 6 show the illustration of the preparation of the $MoSi_2$-$TaSi_2$-borosilicate glass porous coating, the porous fibrous ZrO_2 ceramic are surround by raw material consisted of $MoSi_2$, $TaSi_2$ and borosilicate glass, and part original coating composition has permeated into the substrate. In the sintering process, the top surface coating composition will react with oxygen to form a uniform Ta-Si-O compound glass layer that resists further oxidation. The borosilicate glass in the inner coating will be molten and connect with $MoSi_2$ and $TaSi_2$ particles together, as well as the fibrous ZrO_2 ceramic, which will build a strong bonding between the coating and the substrate.

2.2. The radiation property of the coating

Fig. 7 (a) and (b) shows the spectral reflectivity and emissivity in the wavelength range of 0.3–2.5 μm and 2.5–15 μm of the $MoSi_2$–$TaSi_2$–borosilicate glass coating, respectively. As shown, the spectral reflectivity curves present low reflectivity values both in UV–vis–NIR and middle–infrared range. In the wavelength range of 0.3–2.5 μm, with the increase in the wavelength, the reflectivity gradually increases and the emissivity reduces from 0.9 to 0.85. The step–like spectral reflectivity curve is similar to that of the binary carbide and boride ultra–high temperature ceramics [33,34], which is attributed to their semi-metal electronic structures [35].

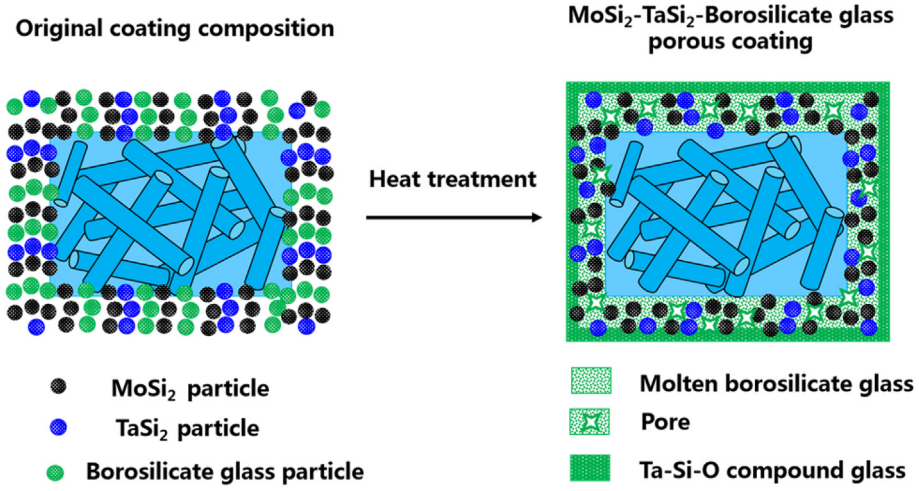

Fig. 6. Illustration of the preparation of the $MoSi_2$-$TaSi_2$-borosilicate glass porous coating.

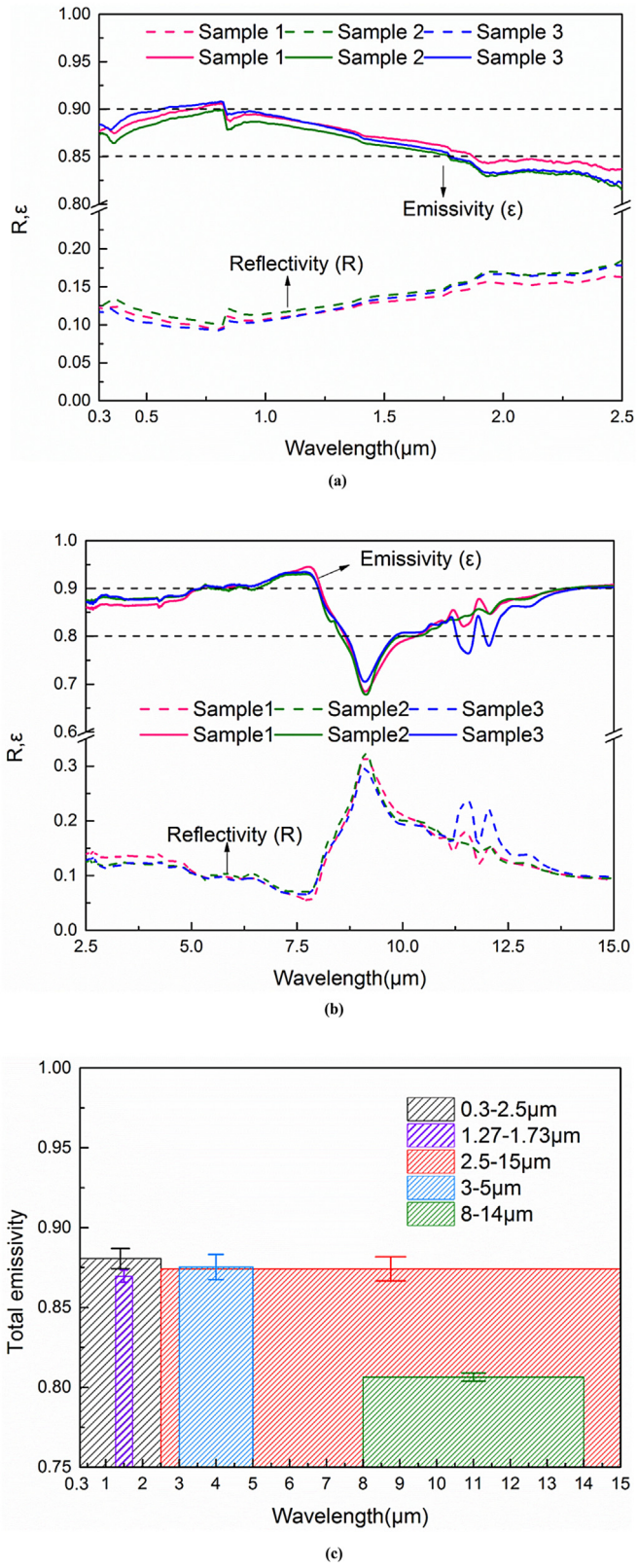

Fig. 7. (a) The spectral reflectivity and emissivity of the $MoSi_2$–$TaSi_2$–borosilicate glass coating in the wavelength range of 0.3–2.5 μm (b) 2.5–15 μm (c) Histogram of the calculated total emissivity in various wavelengths.

According to the Plank's law, when the blackbody temperature is at 1273 K, 97% of the electromagnetic energy emitted by a blackbody in thermal equilibrium is below 14 μm, and 76% is below 5 μm. Fig. 7(c) shows the histogram of the calculated total emissivity in various wavelengths. In the range of 0.3–2.5 μm, the total emissivity is higher than 0.88, and the emissivity is about 0.87 in the range of 3–5 μm, while in the range of 8–14 μm, the emissivity is only 0.8. In fact, an ideal blackbody at 1400 K emits nearly 5% of its energy in the band 8–14 μm [36]. According to Wien's displacement law, $\lambda_{max} = b/T$, $b = 2.8977721(26) \times 10^{-3}$ m K; the blackbody intensity is maximum at a given temperature at wavelength λ_{max}, and this maximum shifts toward shorter wavelengths as the temperature is increased. Therefore, the higher the temperature, the more meaningful the emissivity of the short wavelength. When the temperature is in the range of 1673 K and 2273 K, the largest radiation wavelength shifts from approximately 1.73 to 1.27 μm; in the range of the wavelength, the $MoSi_2$–$TaSi_2$–borosilicate glass coating exhibits a high emissivity greater than 0.86.

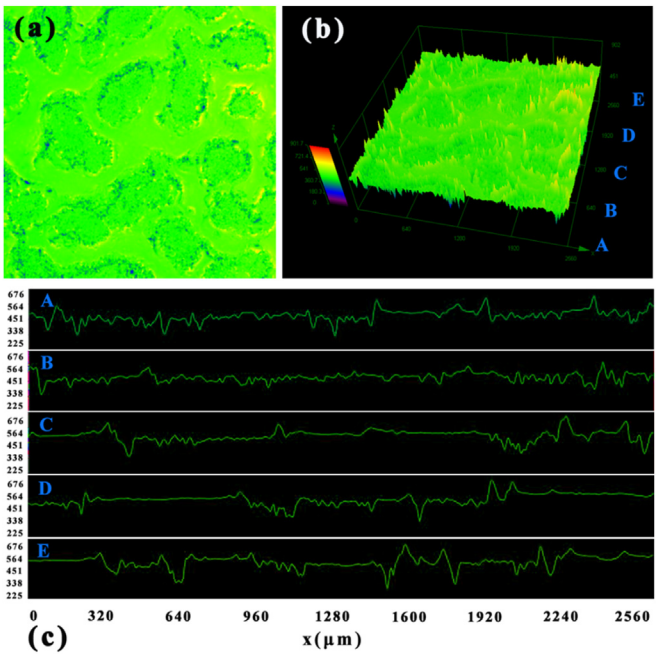

Fig. 8. (a) The surface roughness morphology of the coating (b) 3D surface roughness morphology gradient map of the coating (c) The line roughness profiles of different positions marked in (b).

It is well known that not only the surface chemical composition, but also the surface morphology has a great influence on the emissivity of the coatings. It was reported that there is a positive link between the emissivity and the surface roughness [37–39]. Fig. 8 shows the surface roughness morphology and 3D surface roughness morphology gradient map of the coating (a partial view of 2560 μm × 2560 μm is shown in order to better highlight surface defects). Besides, the line profiles and roughness values of five different locations marked in Fig. 8(b) are presented in Fig. 8(c) and summarized in Table 1, respectively, which are obtained from a CLSM study. Wen et al. [40] divided the rough surfaces into three

Table 1
The roughness values of five different locations.

Location	Rq (μm)	Rsk (μm)	σ/λ(λ < 10 μm)
A	15.789	−0.223	>1
B	12.692	−0.091	>1
C	11.624	0.033	>1
D	10.640	−0.246	>1
E	12.862	0.243	>1

spectral regions based on optical roughness, which is represented by the ratio of root–mean–square (Rq) surface roughness, σ, to wavelength, λ; namely: (1) Specular Region ($0<\sigma/\lambda < 0.2$); (2) Intermediate Region ($0.2<\sigma/\lambda < 1$); and (3) Geometric Region ($\sigma/\lambda > 1$). For the different locations marked with A, B, C, D, E of $MoSi_2$–$TaSi_2$–borosilicate glass coating surface, the σ/λ ratio is greater than 1 in the region of ultraviolet to near infrared (λ = 0.1–10 μm). Hence, the σ/λ ratio of the coating lies in the Geometric Region. In the Geometric Region, surfaces with a repeatable grooved finish, such as V–shaped grooves, circular grooves, and pyramidal grooves are commonly used to model the emissivity enhancement. Combining the line roughness profiles shown in Fig. 8(c), "V–shaped grooves" model is more suitable to explain the phenomena of the enhanced emissivity for the coating. As we know, most of the electromagnetic wave was reflected, and only a little was absorbed by the coatings with a smooth surface. However, a significant absorptivity increase and reflectivity decrease by small gradual slopes in "V–shaped grooves" can be observed from the rough coating because multiple reflection will be caused by the slope of the "V–shaped grooves" surface. Therefore, compared with the smooth surface, the rough coatings exhibit lower reflectivity and higher absorptivity, which leads to high emissivity according to Kirchhoff's law of thermal radiation.

2.3. Thermal shock behavior

The weight change curve of $MoSi_2$-$TaSi_2$-borosilicate glass coated sample during the thermal shock test between 1673 K and room temperature is shown in Fig. 9. The initial weight gain is observed in the coated sample, with a maximum of 1% after the first thermal shock cycle, then a continuous weight loss occurs, and the cumulated weight loss of the coated sample is only 2.38% after 10 cycles, which shows the stable thermal cycling oxidation resistance.

Fig. 10 shows the XRD pattern of $MoSi_2$-$TaSi_2$-borosilicate glass coated sample after 10 cycles. It can be found that $MoSi_2$, SiO_2, Ta_2O_5 are the main components on the surface. Ta_2O_5 and partial SiO_2 are generated form the oxidation of $TaSi_2$, which results in the initial weight gain during the thermal shock test. Compared to the original components on the surface of the coating (Fig. 3(b)), the peaks of $MoSi_2$, Mo and Mo_5Si_3 phases have decreased, it is because that these phases are depleted slowly with the formation of volatilizable products (MoO_3) according to Eqs. (6), (11) and (12), resulting in the continuous weight loss of the coated samples. Moreover, a new $NaTaMoO_6$ phase is detected on the surface, which can be inferred according to Eq. (13).

$$Mo_5Si_3(s) + 21/2O_2(g) = 5MoO_3(g) + 3SiO_2(s) \quad (11)$$

$$Mo(s) + 3/2O_2(g) = MoO_3(g) \quad (12)$$

$$Na_2MoO_4(s) + MoO_3(s) + Ta_2O_5(s) = 2NaTaMoO_6(s) \quad (13)$$

Fig. 11 displays the surface SEM image of $MoSi_2$-$TaSi_2$-borosilicate glass coating after 10 thermal shock cycles. No macro cracks are observed on the surface (Fig. 11(a)), and some crystalline like and rod like phase acted as the "immiscible phase" generate in the surface of the coating, which forms a kind of "inlaid structure". Fig. 11(b) and (c) show the magnification of region A and B in Fig. 11(a). Combined with EDS (Fig. 11(d), (e) and (f)) and XRD (Fig. 10) analyses, spot 1, spot 2 and spot 3 could be distinguished as Ta_2O_5, SiO_2 and Ta_2O_5 respectively. It could be inferred that SiO_2 content in glass and glass melting temperature will gradually increase as B_2O_3 evaporates form original borosilicate glass and SiO_2 generated form the oxidized $TaSi_2$ with increasing thermal shock cycles, which results in the formed compound glass. The generated crystalline SiO_2 improve the viscosity of the compound glass, leading to the micro cracks couldn't be sealed.

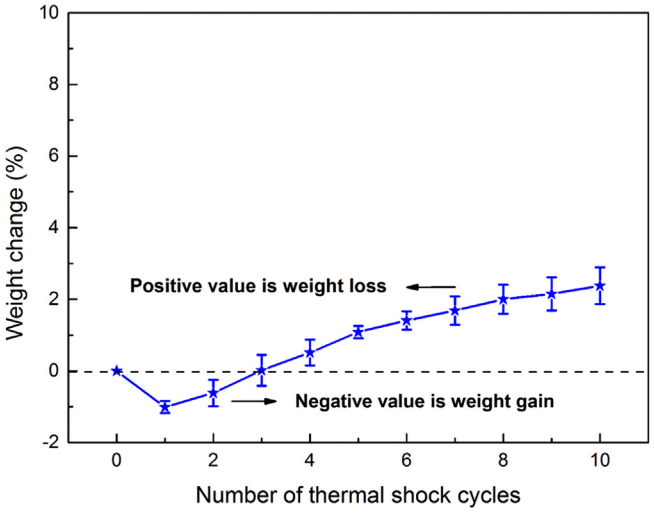

Fig. 9. Weight change curve of $MoSi_2$-$TaSi_2$-borosilicate glass coated samples after 10 thermal shock cycles.

Fig. 12(a) shows the cross-section SEM images of $MoSi_2$ –$TaSi_2$ – borosilicate glass coated fibrous ZrO_2 ceramic. It could be divided into two layers of the coating: the surface coating layer (zone I) and the interfacial transition layer (zone II). The surface coating layer presents a dense and crack free structure with the thickness of approximately 120 μm, which is clearly shown in magnified SEM image (Fig. 12(b)). During the thermal shock test process, the porous coating gradually transforms into a dense coating, which is attributed to the viscous flow of molten borosilicate glass. Fig. 12(c) shows the magnification of region B in Fig. 12(a), the interfacial transition layer is a fiber reinforced composite and presents an interlocking structure, which contributed to the tight bond between the coating and substrate.

It was reported that the coating stress σ_c may be divided into three components: $\sigma_c = \sigma_t + \sigma_g + \sigma_a$, where σ_t is the CTE mismatch

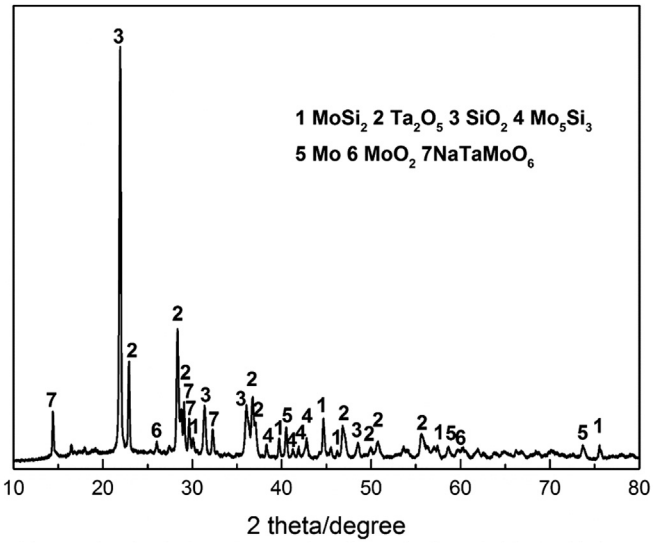

Fig. 10. XRD patterns of $MoSi_2$-$TaSi_2$-borosilicate glass coating surfaces after 10 thermal shock cycles.

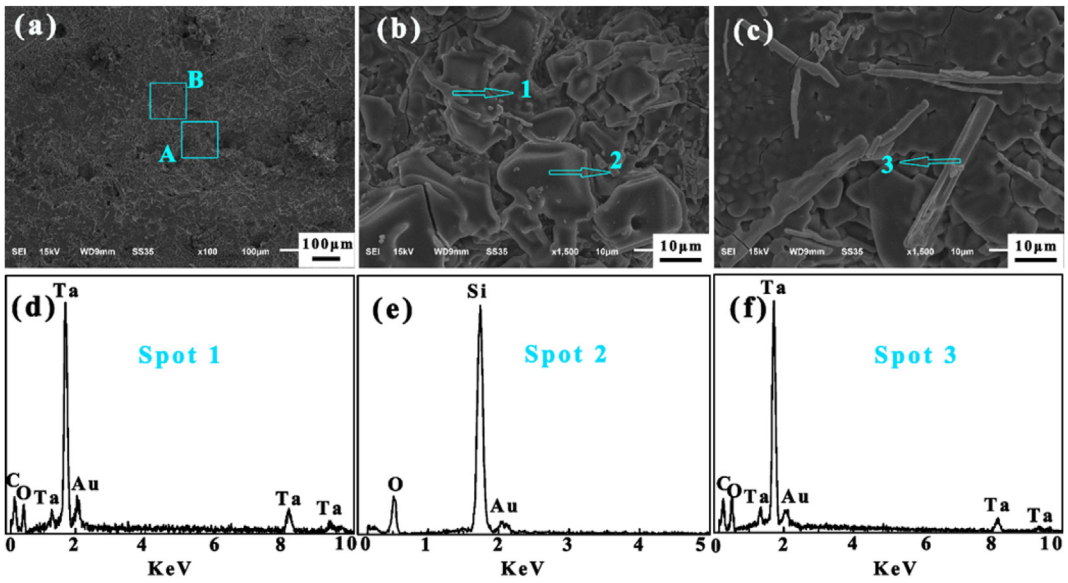

Fig. 11. (a) Surface SEM image of $MoSi_2$-$TaSi_2$-borosilicate glass coating after 10 thermal shock cycles; (b) magnification of region A in (a); (c) magnification of region B in (a); (d–f) EDS analysis of the coating.

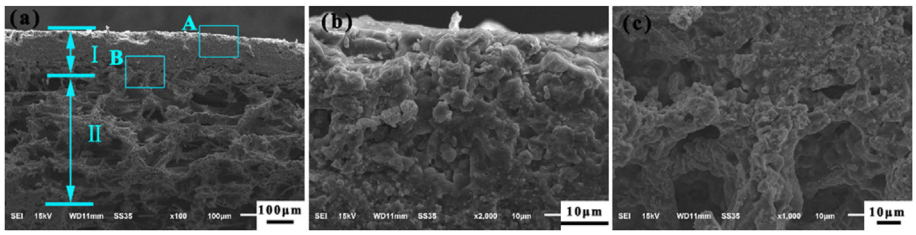

Fig. 12. (a) Cross section SEM image of $MoSi_2$-$TaSi_2$-borosilicate glass coating after 10 thermal shock cycles; (b) magnification of region A in (a); (c) magnification of region B in (a).

stress, σ_g is the growth stress and σ_a is the aging stress [41]. The growth stress is a stress that develops during the coating deposition. The aging stress is a stress that results from many aspects such as phase transformation, sintering, oxidation and chemical reactions of the coating. In this work, the coating stress may consist mainly of the CTE mismatch stress and the aging stress. Fig. 13 shows the variations in thermal expansion rate with the temperature for $MoSi_2$, $TaSi_2$ and fibrous ZrO_2 ceramic, the average CTEs are 9.32×10^{-6}/K, 9.78×10^{-6}/K and 10.2×10^{-6}/K, which shows a little mismatch between the coating and the substrate in consideration of the borosilicate glass composition in the coating, causing the CTE mismatch stress. During the process of thermal shock test, the samples will suffer quick heating and cooling, the aging stress is formed due to the oxidation of the coating materials during the thermal shock test. Then, the volume ratio, r_V, of the converted coating products to the initial coating is:$r_V = \frac{[2MW_{Ta_2O_5}/\rho_{Ta_2O_5} + 8MW_{SiO_2}/\rho_{SiO_2}]}{4MW_{TaSi_2}/\rho_{TaSi_2}}$, where MW is the molecular weight and ρ is weight density of each species. The molecular weights of $TaSi_2$, Ta_2O_5 and SiO_2 are 237.13, 441.89 and 60.084, respectively and the density of $TaSi_2$, Ta_2O_5 and SiO_2 are 9.14 g/cm^3, 8.2 g/cm^3 and 2.2 g/cm^3, respectively. Thus, the conversation of $TaSi_2$ to Ta_2O_5 and SiO_2 will correspond to a total increase of the coating volume by 314%, which will lead to stresses in the coating, once the coating stress accumulated enough, the micro cracks appear in the surface of the coating, the presence of these micro cracks provide the inward diffusion channels for the oxygen, and thus progressively accelerate the oxidation and the failure of the coating. However, no destructive micro cracks are detected during the thermal shock test, which can be briefly inferred as the porous structure of the coating and the similar thermal expansion coefficient between the coating materials and the substrate.

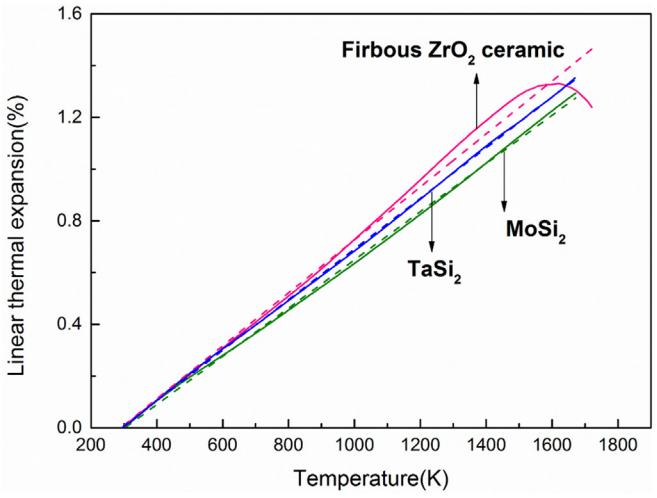

Fig. 13. Variations in thermal expansion rate with the temperature for $MoSi_2$, $TaSi_2$ and fibrous ZrO_2 ceramic.

3. Conclusion

A high emissivity $MoSi_2$-$TaSi_2$-borosilicate glass porous coating was designed and successfully developed on the low thermal conductivity fibrous ZrO_2 ceramic by slurry dipping and subsequent rapid sintering method. The as-prepared coating maintains a top Ta-Si-O compound glass layer and a porous $MoSi_2$-$TaSi_2$-borosilicate glass inner layer. The total emissivity of the $MoSi_2$-$TaSi_2$-borosilicate glass porous coating is up to 0.88 in the range of 0.3–2.5 μm and 0.87 in the range of 2.5–15 μm at room temperature. The coating is without macro crack and spallation, turning into a dense structure in the surface layer and presenting an interlocking structure in the interfacial layer after thermal cycling between 1673 K and room temperature 10 times, which was attributed to the synergistic effect of porous structure and the match of thermal expansion coefficient between the coating and substrate. Thus, the high emissivity $MoSi_2$-$TaSi_2$-borosilicate glass porous coating with high temperature resistance presented a promising potential for application in thermal insulation materials.

Acknowledgment

This work was financially supported by the Program for Changjiang Scholars and Innovative Research Team in University (No. IRT_15R35), the Industry Program of Science and Technology Support Project of Jiangsu Province (No.BE2014128), the National Aeronautical Science Foundation of China (No.201452T4001), the Major Program of Natural Science Fund in Colleges and Universities of Jiangsu Province (No.15KJA430005), the Prospective Joint Research Program of Jiangsu Province (No.BY2015005–01), the Priority Academic Program Development of Jiangsu Higher Education Institutions (PAPD), Project Funded by China Postdoctoral Science Foundation (2015M570442).

References

[1] D.B. Leiser, R. Churchward, V. Katvala, D. Stewart, A. Balter, Advanced porous coating for low-density ceramic insulation materials, J. Am. Ceram. Soc. 72 (1989) 1003–1010.
[2] D.B. Leiser, D.A. Stewart, Toughened uni-piece, fibrous, reinforced, oxidization-resistant composite, U. S. patent. 7,314,648 B1, 2008.
[3] J. He, X. Li, D. Su, H. Ji, Y. Qiao, High-strength mullite fibers reinforced ZrO_2–SiO_2 aerogels fabricated by rapid gel method, J. Mater. Sci. 50 (2015) 7488–7494.
[4] Y. Kong, Y. Zhong, X. Shen, S. Cui, M. Fan, Preparation of fiber reinforced porous silicon carbide monoliths, Mater. Lett. 110 (2013) 141–143.
[5] A.O. Barney, V. Heng, K.S. Oka, M. Santos, A.A. Zinn, M. Droege, Hybrid aerogel rigid ceramic fiber insulation and method of producing same, US 6,770,584 B2, 2004.
[6] J. Sun, Z. Hu, J. Li, H. Zhang, C. Sun, Thermal and mechanical properties of fibrous zirconia ceramics with ultra-high porosity, Ceram. Int. 40 (2014) 11787–11793.
[7] D. Alfano, L. Scatteia, S. Cantoni, M. Balat-Pichelin, Emissivity and catalycity measurements on SiC-coated carbon fibre reinforced silicon carbide composite, J. Eur. Ceram. Soc. 29 (2009) 2045–2051.
[8] D.M. Van Wie, D.G. Drewry, D.E. King, C.M. Hudson, The hypersonic environment: required operating conditions and design challenges, J. Mater. Sci. 39 (2004) 5915–5924.
[9] X. He, Y. Li, L. Wang, Y. Sun, S. Zhang, High emissivity coatings for high temperature application: progress and prospect, Thin. Solid. Films 517 (2009) 5120–5129.
[10] G. Schultes, M. Schmitt, D. Goettel, O. Freitag Weber, Strain sensitivity of TiB_2, $TiSi_2$, $TaSi_2$ and WSi_2 thin films as possible candidates for high temperature strain gauges, Sens. Actuat. A-Phys. 126 (2006) 287–291.
[11] Q. Fu, Y. Shan, C. Cao, H. Li, K. Li, Oxidation and erosion resistant property of SiC/Si–Mo–Cr/$MoSi_2$ multi-layer coated C/C composites, Ceram. Int. 41 (2015) 4101–4107.
[12] T. Feng, H.J. Li, Q.G. Fu, X. Yang, H. Wu, The oxidation behavior and mechanical properties of $MoSi_2$–$CrSi_2$–SiC–Si coated carbon/carbon composites in high-temperature oxidizing atmosphere, Corros. Sci. 53 (2011) 4102–4108.
[13] Y.L. Zhang, J. Ren, S. Tian, H. Li, X. Ren, Z. Hu, HfC nanowire-toughened $TaSi_2$-TaC-SiC-Si multiphase coating for C/C composites against oxidation, Corros. Sci. 90 (2015) 554–561.
[14] X. Ren, H. Li, Q. Fu, Y. Chu, K. Li, Oxidation resistant graded multiphase coating for carbon/carbon composites, Surf. Coat. Technol. 232 (2013) 821–826.
[15] S.A. Ghaffari, M.A. Faghihi-Sani, F. Golestani-Fard, H. Mandal, Spark plasma sintering of TaC-HfC UHTC via disilicides sintering aids, J. Eur. Ceram. Soc. 33 (2013) 1479–1484.
[16] D. Sciti, G. Bonnefont, G. Fantozzi, L. Silvestroni, Spark plasma sintering of HfB_2 with low additions of suicides of molybdenum and tantalum, J. Eur. Ceram. Soc. 30 (2010) 3253–3258.
[17] G. Shao, X. Wu, Y. Kong, S. Cui, X. Shen, C. Jiao, J. Jiao, Thermal shock behavior and infrared radiation property of integrative insulations consisting of $MoSi_2$/borosilicate glass coating and fibrous ZrO_2 ceramic substrate, Surf. Coat. Technol. 270 (2015) 154–163.
[18] G. Shao, X. Wu, Y. Kong, X. Shen, S. Cui, X. Guan, C. Jiao, J. Jiao, Microstructure, radiative property and thermal shock behavior of $TaSi_2$–SiO_2-borosilicate glass coating for fibrous ZrO_2 ceramic insulation, J. Alloy. Compd. 663 (2016) 360–370.
[19] M. Wang, X. Li, D. Su, H. Ji, H. Tang, Z. Zhao, J. He, Effect of glass phase content on structure and properties of gradient $MoSi_2$–BaO–Al_2O_3–SiO_2 coating for porous fibrous insulations, J. Alloy. Compd. 657 (2016) 684–690.
[20] X. Ren, H. Li, Q. Fu, K. Li, $Ta_xHf_{1-x}B_2$-SiC multiphase oxidation protective coating for SiC-coated carbon/carbon composites, Corros. Sci. 87 (2014) 479–488.
[21] J. Sun, Q.G. Fu, L.P. Guo, Y. Liu, C.X. Huo, H.J. Li, Effect of filler on the oxidation protective ability of $MoSi_2$ coating for Mo substrate by halide activated pack cementation, Mater. Des. 92 (2016) 602–609.
[22] Y. Niu, L. Huang, C. Zhai, Y. Zeng, X. Zheng, C. Ding, Microstructure and thermal stability of $TaSi_2$ coating fabricated by vacuum plasma spray, Surf. Coat. Technol. 279 (2015) 1–8.
[23] Y. Niu, H. Wang, Z. Liu, C. Hu, X. Wang, X. Zheng, C. Ding, Microstructure evolution of ZrB_2–$MoSi_2$ composite coatings at middle and high temperatures, Surf. Coat. Technol. 273 (2015) 30–38.
[24] G. Shao, X. Wu, S. Cui, X. Shen, Y. Kong, Y. Lu, C. Jiao, J. Jiao, High emissivity $MoSi_2$–ZrO_2–borosilicate glass multiphase coating with SiB_6 addition for fibrous ZrO_2 ceramic, Ceram. Int. 42 (2016) 8140–8150.
[25] B. Xu, C. Hong, Q. Qu, X. Zhang, J. Han, N. Li, K. Gui, G. Zhao, C. Liu, Preparation of a multi-composition coating for oxidation protection of modified carbon-bonded carbon fiber composites by a rapid sintering method, Surf. Coat. Technol. 270 (2015) 109–116.
[26] T. Feng, H.J. Li, M.H. Hu, H.J. Lin, L. Li, Oxidation and ablation resistance of Fe_2O_3 modified ZrB_2–SiC–Si coating for carbon/carbon composites, Ceram. Int. 42 (2016) 270–278.
[27] P. Wang, C. Zhou, X. Zhang, G. Zhao, B. Xu, Y. Cheng, P. Zhou, W. Han, Oxidation protective ZrB_2–SiC coatings with ferrocene addition on SiC coated graphite, Ceram. Int. 42 (2016) 2654–2661.
[28] R.S. John, R. Howell, M. Pinar Menguc, in: Thermal Radiation Heat Transfer, fifth ed., CRC Press Inc., Boca Raton, Florida, 2010.
[29] X. Xiao, L. Miao, G. Xu, L. Lu, Z. Su, N. Wang, S. Tanemura, A facile process to prepare copper oxide thin films as solar selective absorbers, Appl. Surf. Sci. 257 (2011) 10729–10736.
[30] S. Le Roux, F. Deschaux-Beaume, T. Cutard, P. Lours, Quantitative assessment of the interfacial roughness in multi-layered materials using image analysis: application to oxidation in ceramic-based materials, J. Eur. Ceram. Soc. 35 (2015) 1063–1079.
[31] J.S. Park, R. Sakidja, J.H. Perepezko, Coating designs for oxidation control of Mo–Si–B alloys, Scr. Mater. 46 (2002) 765–770.
[32] I.G. Talmy, J.A. Zaykoski, M.M. Opeka, High-temperature chemistry and oxidation of ZrB_2 ceramics containing SiC, Si_3N_4, Ta_5Si_3, and $TaSi_2$, J. Am. Ceram. Soc. 91 (2008) 2250–2257.
[33] D. Sciti, L. Silvestroni, L. Mercatelli, J.L. Sans, E. Sani, Suitability of ultra-refractory diboride ceramics as absorbers for solar energy applications, Sol. Energy Mat. Sol. C 109 (2013) 8–16.
[34] Z. Fang, C. Lu, C. Guo, Y. Lu, D. Gao, Y. Ni, J. Kou, Z. Xu, P. Li, Suitability of layered Ti_3SiC_2 and $Zr_3[Al(si)]_4C_6$ ceramics as high temperature solar absorbers for solar energy applications, Sol. Energy Mat. Sol. C 134 (2015) 252–260.
[35] E. Sani, L. Mercatelli, P. Sansoni, L. Silvestroni, D. Sciti, Spectrally selective ultra-high temperature ceramic absorbers for high-temperature solar plants, J. Renew. Sustain. Energy 4 (2012) 033104.
[36] E. Sani, L. Mercatelli, F. Francini, J.L. Sans, D. Sciti, Ultra-refractory ceramics for high-temperature solar absorbers, Scr. Mater. 65 (2011) 775–778.
[37] D.B. Mahadik, S. Gujjar, G.M. Gouda, H.C. Barshilia, Double layer SiO_2/Al_2O_3 high emissivity coatings on stainless steel substrates using simple spray deposition system, Appl. Surf. Sci. 299 (2014) 6–11.
[38] B. Rousseau, M. Chabin, P. Echegut, A. Sin, F. Weiss, P. Odier, High emissivity of a rough Pr_2NiO_4 coating, Appl. Phys. Lett. 79 (2001) 3633–3635.
[39] E. Brodu, M. Balat-Pichelin, J.L. Sans, M.D. Freeman, J.C. Kasper, Efficiency and behavior of textured high emissivity metallic coatings at high temperature, Mater. Des. 83 (2015) 85–94.
[40] C.D. Wen, I. Mudawar, Modeling the effects of surface roughness on the emissivity of aluminum alloys, Int. J. Heat. Mass. Tran. 49 (2006) 4279–4289.
[41] K.N. Lee, J.I. Eldridge, R.C. Robinson, Residual stresses and their effects on the durability of environmental barrier coatings for SiC ceramics, J. Am. Ceram. Soc. 88 (2005) 3483–3488.